Quantum size effects in the surface energy of Pb/Si(111) film nanostructures studied by surface x-ray diffraction and model calculations

P. Czoschke,[1,2] Hawoong Hong,[2] L. Basile,[1,2] and T.-C. Chiang[1,2,*]

[1]*Department of Physics, University of Illinois at Urbana-Champaign, 1110 W. Green Street, Urbana, Illinois 61801-3080*

[2]*Frederick Seitz Materials Research Laboratory, University of Illinois at Urbana-Champaign, 104 S. Goodwin Avenue, Urbana, Illinois 61801-2902*

(Dated: April 18, 2005)

We have used surface x-ray diffraction from a synchrotron source, along with models based upon a free-electron gas confined to a quantum well, to study quantum size effects in the surface energy of ultrathin Pb films grown on pretreated Si(111) substrates. Films grown at 110 K are smooth, but as they are annealed to near room temperature, their morphology is observed evolving through various metastable states and eventually to a roughened state in local equilibrium. Strong variations in the stability of different island heights are observed, consistent with quasibilayer oscillations in the surface energy found from the theoretical free-electron calculations. By analyzing the quasi-equilibrium distribution of thicknesses, empirical information on the film surface energy is obtained for a wide range of thicknesses. The morphological annealing behavior of the films is also found to be explained by the deduced surface energy.

PACS numbers: 68.35.Md, 61.10.Kw, 73.21.Fg, 68.55.Jk, 68.65.Fg

I. INTRODUCTION

A fundamental understanding of non-classical effects in atomic-scale metallic structures is critical for the successful development and creation of future nanodevices. Due to quantization of the allowed electronic states in a metallic nanostructure, electron standing waves form that interact with the discrete nature of the atomic lattice. Such effects due to quantum confinement can lead to a high degree of size dependence in a multitude of different properties of the system, including its lattice structure, transport characteristics, thermal stability, work function, superconducting transition temperature, electron-phonon coupling, electronic structure, surface charge density, growth behavior and morphology, chemical reactivity, and surface energy.[1–45] To further understand such effects, it is useful to start with a system in which only one of the three spatial dimensions has a length scale in the quantum regime. Thin films and quasi-two-dimensional nanostructures fall into this category and are the subject of this study.

The relative stability of thin metal films has been shown to exhibit strong variations as a function of thickness that have been attributed to electronic contributions to the surface energy.[38,41–43] In addition, for certain temperature ranges, some systems exhibit a peculiar film morphology where steep-sided, flat-topped islands of uniform height form on the surface. Using x-ray diffraction and scanning tunneling spectroscopy, the formation of these "nanomesas" has been correlated with the electronic structure of the films.[17–23,42,43] Thus, evidence for electronic effects in specific film thicknesses has been reported, but comprehensive empirical information on the surface energy over a broad range of thicknesses is lacking. The technique of x-ray diffraction is well-equipped to provide such measurements since it both measures absolute film thicknesses and provides a statistical sampling over a macroscopic area. By preparing a sample that is near thermal equilibrium, a broad range of thicknesses will be present on the sample that reflects the local energy landscape of the system. The distribution of thicknesses can be measured using x-ray diffraction to obtain the relative film stability as a function of thickness, which is related to the surface energy. We presented a limited study in a previous work.[43] Here we provide a comprehensive analysis of a larger data set and offer a detailed model analysis.

The experiment is a surface x-ray diffraction study of the structural evolution of smooth Pb films grown on Si(111) at 110 K as they are annealed to a state of local equilibrium near room temperature. By frequently interrupting the annealing process and examining the film morphology, we effectively watch the system explore the local energy landscape as it evolves. Detailed discussions are presented for two different samples, one with an initial thickness that corresponds to a relatively stable configuration (low surface energy), and one whose initial thickness is relatively unstable (high surface energy). The structural evolution and thermal stability of the two films differ markedly; however, analysis of their final quasi-equilibrium states produces the same form for the surface energy, as expected. The annealing behavior of the films also reveals an additional effect; namely, after the initially smooth film breaks up, further annealing results in the formation of increasingly taller islands. This effect is also attributed to quantum electronic effects. First principles calculations show that the most energetically favored configuration of the system consists of a single layer wetting the substrate;[42] however, due to the initial volume of deposited film material, in order to conserve mass the film morphology phase separates into surface regions covered only by a wetting layer, which

has the lowest surface energy, and regions with islands of various heights. As the annealing temperature increases, the system has more thermal energy with which to rearrange the atoms on the surface, resulting in the formation of taller islands and a corresponding increase in the area covered by the wetting layer.

Previous photoemission and scanning tunneling spectroscopy studies of Pb/Si(111) nanomesas show that the stability of islands of different heights is correlated with the gap between the highest occupied subband and the Fermi level.[19,23,35,38,41] To elucidate the origin of this effect and develop a more complete understanding of the energetics involved, we develop a model for the surface energy of a metal film based upon a free-electron gas confined to an infinite quantum well. Such a model shows strong oscillations in the surface energy that dampen with increasing thickness and that have a wavelength of half the Fermi wavelength, which is characteristic of quantum size effect phenomena. The origin of this periodicity is discussed with relation to the subband structure that arises due to quantum confinement of the itinerant electrons in the metal film. When sampled at thicknesses of integer atomic layers of Pb, bilayer oscillations in the surface energy are apparent that indicate a preference for either even or odd thicknesses, with alternations between the two following a superperiodic beating pattern. For comparison, a similar model that replaces the infinite potential boundaries of the quantum well with finite barriers is developed in the Appendix and compared to the infinite well model, the results from which are found to be equivalent. The form for the surface energy found from the theoretical models is consistent with the empirically derived stability data from the Pb/Si(111) samples and is used, in conjunction with the data, to extract quantitative information on the surface energy of the Pb films as a function of thickness.

II. EXPERIMENT

The experiments were conducted using 19.9 keV x rays obtained from an undulator source at UNICAT (University, National Laboratory, Industry Collaborative Access Team), Sector 33ID, Advanced Photon Source, Argonne National Laboratory. Diffraction data were obtained using a six-circle goniometer integrated with an ultrahigh vacuum chamber that has a base pressure of 6×10^{-11} torr. A channel-cut double-Si(111) crystal monochromator was used to select the x-ray energy and perform sagittal focusing while vertical focusing and harmonic rejection was accomplished with a pair of Rh-striped mirrors. The 10×40 mm substrates were cut from P-doped commercial wafers with a nominal resistivity of 1–30 Ω·cm and mounted to a manipulator cooled with liquid nitrogen. The sample was thermally anchored to the manipulator with a sapphire block while a tantalum clip provided electrical contact for direct current heating. In addition, a tungsten coil behind the sample provided an indirect heat source for low-temperature annealing. The sample temperature was measured by a pair of thermocouples attached to the tantalum mounting clips at both ends of the sample. Quoted temperatures are the average of the two readings, with errors in the sample temperature ranging from approximately $\pm 5^\circ$ at base temperature (110 K) up to $\pm 20^\circ$ at the highest annealing temperatures (300 K). Discrepancies in the readings of the two thermocouples indicated the presence of a thermal gradient across the sample; however, due to the small footprint of the beam — about 0.5 mm parallel to the thermal gradient — compared to the 40 mm length of the sample, the measured region of the sample can be considered to be of uniform temperature, with the above errors representing the confidence interval of the absolute temperature.

After mounting in the vacuum chamber, the substrates were subjected to prolonged outgassing at 600°C. The clean Si(111) surface was then obtained by flashing the substrate to 1250°C for approximately 13 seconds, which reliably resulted in a high quality 7×7 reconstruction as verified by reflection high energy electron diffraction and x-ray diffraction. The surface was then pretreated by depositing 4.5 Å Pb on it by thermal evaporation from a Knudsen cell, followed by a 10 minute anneal at 415°C to desorb the excess Pb and form the Pb/Si(111)-$(\sqrt{3} \times \sqrt{3})R30^\circ$ phase with an initial coverage of approximately $\frac{4}{3}$ monolayer in Si(111) units. This pretreatment has been shown to result in bulklike termination of the Si(111) interface upon which smooth Pb films can be grown at low temperatures.[38,46,47] During the initial stages of deposition, the interface reconstruction disappears, being replaced by a wetting layer of bulklike density on the substrate. In our discussion below, this single Pb wetting layer is included as part of the total thickness or coverage of a film.

Pb films were grown *in situ* at 110 K using molecular beam epitaxy at a rate of 0.84 Å/min. At this temperature the system is known to follow a metastable layer-by-layer growth mode that allows for monitoring of the coverage of the films during deposition by collecting the reflected x-ray intensity at the lowest-order out-of-phase condition for Pb(111), which exhibits layer-by-layer oscillations.[47] After deposition, the films were slowly annealed to progressively higher temperatures in increments of approximately 5–10 K. After resting at each desired annealing temperature for ∼5 minutes, the sample was quenched back to 110 K for measurement of the specular extended x-ray reflectivity, which was obtained either by doing a series of ω scans ("rocking curves") at different values of perpendicular momentum transfer or by doing a set of "ridge scans" on and parallel to the specular condition along the rod. Both of these methods allow for effective integration and background subtraction of the specularly reflected intensity and were found to be equivalent for the range of momentum transfer studied.

III. ANALYSIS

A. Specular x-ray reflectivity

From previous x-ray diffraction and microscopy studies,[17–19,21–23,42] it is known that Pb films grown on Si(111) at temperatures around 150–200 K exhibit a peculiar morphology in which uniform-height islands form whose lateral extents can be hundreds of nanometers. Between these islands is a single layer of Pb wetting the substrate. Since in this study we anneal the films through this temperature range, it is appropriate to expect to encounter the same surface morphology. In addition, detailed analysis of x-ray diffraction data from smooth Pb films has shown that oscillations in the electronic charge density (see Sec. III B and Appendix) near the film interfaces result in significant lattice distortions in the boundary regions of the films.[43,47] These effects must be accounted for in the analysis of the x-ray data.

The x-ray reflectivity was analyzed using a standard kinematic model.[48–51] Since no in-plane components of momentum transfer are included in the specular reflectivity, the lateral structure of the sample does not contribute to the measured intensity. For any sample, there will be regions of different thicknesses. If the distances between these regions is sufficiently small, the integrated intensity is proportional to the coherent sum of the contributions from the substrate and all the Pb overlayers

$$I_{\rm coh}(q_z) \propto \mathcal{C}\left|F_{\rm Si}(q_z)+F_{\rm Pb}(q_z)\right|^2, \tag{1}$$

where $\mathcal{C}$ contains all of the experimental corrections such as the polarization factor, the Lorentz factor, etc.[52] and q_z is the momentum transfer component in the z direction (the surface normal). The substrate contribution is that of a bulk-terminated Si(111) crystal

$$F_{\rm Si}(q_z)=\left(\frac{a_{\rm Pb}}{a_{\rm Si}}\right)^2 f_{\rm Si}(q_z)e^{-M_{\rm Si}}\frac{1+e^{-iq_z a_{\rm Si}\sqrt{3}/12}}{1-e^{-iq_z a_{\rm Si}\sqrt{3}/3}} \tag{2}$$

where $f_{\rm Si}$ and $M_{\rm Si}$ are the atomic scattering factor and the Debye-Waller factor for Si, respectively, and $a_{\rm Si}$ and $a_{\rm Pb}$ are the lattice constants for Si and Pb. The prefactor of $\left(\frac{a_{\rm Pb}}{a_{\rm Si}}\right)^2$ accounts for the different atomic surface densities of Si(111) and Pb(111). Using this convention, Eq. (2) is normalized relative to a Pb(111) atomic layer. The film contribution to the structure factor is then[47]

$$F_{\rm Pb}(q_z)=f_{\rm Pb}(q_z)e^{-M_{\rm Pb}}\sum_N p_N\sum_{j=1}^{N}e^{iq_z z_{j,N}} \tag{3}$$

where p_N is the fractional surface area covered by N Pb layers, the first sum is over all thicknesses present in the film, and $z_{j,N}$ is the position of layer j in a region of thickness N atomic layers (AL) relative to the Si substrate surface. The $z_{j,N}$ parameters were calculated using the lattice distortion model of Refs. 26 and 47 to reflect the aforementioned lattice distortions in the Pb layers due to the Friedel-like oscillations in the electronic charge density. For a closed film, $N \geq 1$,

$$\sum_N p_N = 1, \tag{4}$$

and the total coverage of the film in AL is

$$\Theta = \sum_N N p_N. \tag{5}$$

If regions of different thicknesses are separated by significant lateral distances, the reflected intensity will have a component due to incoherent scattering from these different regions. In the extreme case, where all the thickness regions add up incoherently, the total intensity is the weighted sum of the intensities from each separate region, which consists of a single height island surrounded by a wetting layer. Since the wetting layer fills in the space between the different thickness regions, it will contribute coherently in each case. The integrated intensity in this case is

$$I_{\rm incoh}(q_z) \propto \mathcal{C}\sum_{N>1}\frac{p_N}{1-p_1}\left|F_{\rm Si}(q_z)+F_{\rm Pb}^N(q_z)\right|^2, \tag{6}$$

where the contribution from the Pb overlayers, $F_{\rm Pb}^N$, is the coherent sum of the contributions from all the Pb overlayers in a local region of thickness N AL, including the wetting layer,

$$F_{\rm Pb}^N(q_z) = f_{\rm Pb}(q_z)e^{-M_{\rm Pb}} \times\left[p_1 e^{iq_z z_1}+(1-p_1)\sum_{j=1}^{N}e^{iq_z z_{j,N}}\right]. \tag{7}$$

Note that in the ideal case where the surface consists of islands of only one thickness separated by regions covered only by the wetting layer, Eq. (7) reduces to Eq. (3) and Eq. (6) reduces to Eq. (1); i.e., the incoherent and coherent intensities are equivalent, as one would expect. In actuality, the reflected intensity is likely some combination of coherent and incoherent scattering from regions of different thicknesses, in which case the measured reflected intensity is

$$I(q_z) = \Lambda I_{\rm coh}(q_z) + (1-\Lambda)I_{\rm incoh}(q_z) \tag{8}$$

where Λ is a partial coherence factor ($0 \leq \Lambda \leq 1$), which is treated as a fitting parameter in our analysis.

B. Free-electron model

The essential physics of the surface energy of a metal film can be captured with a model of a free-electron gas confined to an infinite quantum well. In general, the energy of a free-electron gas is

$$E = \frac{2V}{8\pi^3}\int_{|\mathbf{k}|<k_F} d^3\mathbf{k}\frac{\hbar^2|\mathbf{k}|^2}{2m} \tag{9}$$

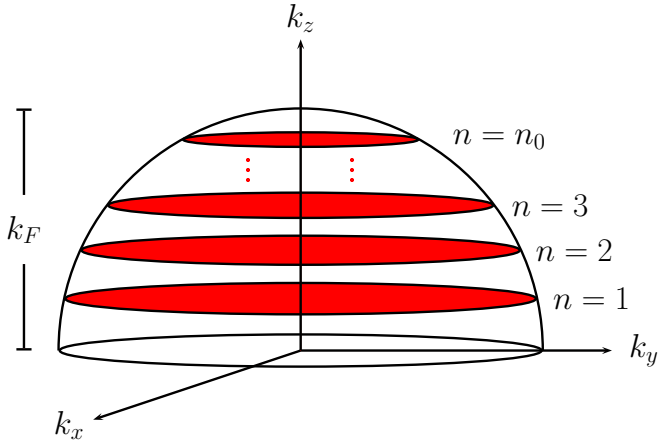

FIG. 1: (Color online) Confinement of the electrons to a quantum well causes the Fermi sphere of allowed states to be reduced to a discrete set of subbands.

where V is the volume of the system, $\hbar$ is Planck's constant divided by 2π, m is the mass of the electron, and k_F is the Fermi wave vector. However, when the gas is confined to a quantum well, the Fermi sphere of allowed states is reduced to a series of subbands, as shown in Fig. 1, indexed by the values

$$k_z = \frac{n\pi}{D} \qquad n = 1, 2, \ldots, n_0 \tag{10}$$

where D is the width of the quantum well and $n_0 = \text{int}\left(\frac{k_F D}{\pi}\right)$ is the quantum number for the highest occupied subband. The total electronic energy of the film then becomes

$$E = \frac{A\hbar^2}{4\pi^2 m} \sum_{n=1}^{n_0} \int_0^{\sqrt{k_F^2 - k_z^2}} 2\pi k_\parallel \left(k_\parallel^2 + k_z^2\right) \, dk_\parallel \tag{11}$$

$$= \frac{A\hbar^2}{8\pi m} \sum_{n=1}^{n_0} \left(k_F^4 - k_z^4\right) \tag{12}$$

$$= \frac{A\hbar^2}{8\pi m} \left[n_0 k_F^4 - \left(\frac{\pi}{D}\right)^4 \frac{1}{30} n_0 (n_0 + 1)(2n_0 + 1)(3n_0^2 + 3n_0 - 1) \right] \tag{13}$$

where A is the surface area of one interface of the film such that $V = DA$. The total energy can be written as

$$E = \varepsilon_b V + 2\varepsilon_s A \tag{14}$$

where ε_b and ε_s are the bulk and surface energy densities, respectively. The factor of two results from the two separate surfaces of our model system slab. The bulk contribution can be found by taking the $D \to \infty$ limit, when boundary effects are negligible. In this limit, we can integrate Eq. (9) without the quantization condition, Eq. (10), to obtain

$$\varepsilon_b = \frac{\hbar^2 \left(k_F^{\text{bulk}}\right)^5}{10\pi^2 m}. \tag{15}$$

Using Eqs. (13) and (14), the surface energy density is then

$$\varepsilon_s = \frac{\hbar^2}{16\pi m} \left[n_0 k_F^4 - \left(\frac{\pi}{D}\right)^4 \left(\frac{1}{5} n_0^5 + \frac{1}{2} n_0^4 + \frac{1}{3} n_0^3 - \frac{1}{30} n_0 \right) - \frac{4}{5\pi} \left(k_F^{\text{bulk}}\right)^5 D \right]. \tag{16}$$

In the simplest case, the width of the quantum well is $D = Nt$, where t is the average interlayer spacing and N is the number of atomic layers in the film. This width is also the extent of the positive uniform background in the jellium model, which we will refer to as the classical width of the film since it ignores any boundary effects and is appropriate in the $D \to \infty$ limit. However, in this case the infinite boundary potentials do not allow any of the electronic charge density to spill past the classical boundaries of the film. Nonetheless, such a scheme represents a reasonable starting point for discussion. A more realistic treatment of the boundary conditions will be introduced later.

As the size of the quantum well gets smaller, the separation between the subbands gets wider and the number of available states decreases. When this happens, the

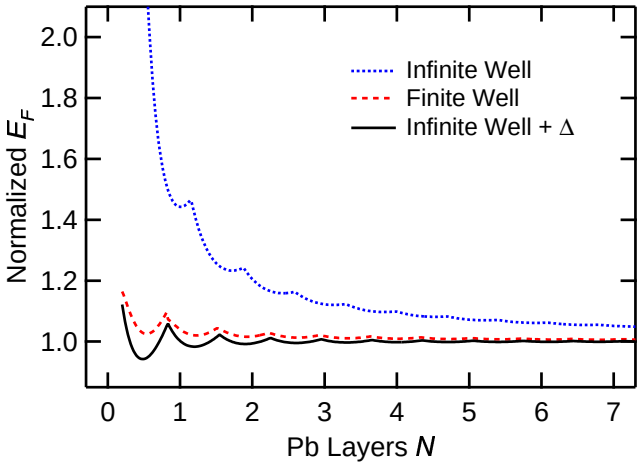

FIG. 2: (Color online) The Fermi energy of a Pb(111) film as a function of thickness, normalized to its bulk free-electron value. In the infinite well model, when the quantum well width is exactly equal to Nt, the Fermi level rises drastically as the film thickness decreases (dotted curve) to compensate for the areas of electron depletion near the film boundaries (see Fig. 3). However, if the electron density is allowed to spill past the classical film boundaries, such compensation is unnecessary and the Fermi level oscillates about its bulk value (solid curve). This Fermi level is very similar to that found in a model where the bounding potentials are finite (dashed curve), which is developed in the Appendix.

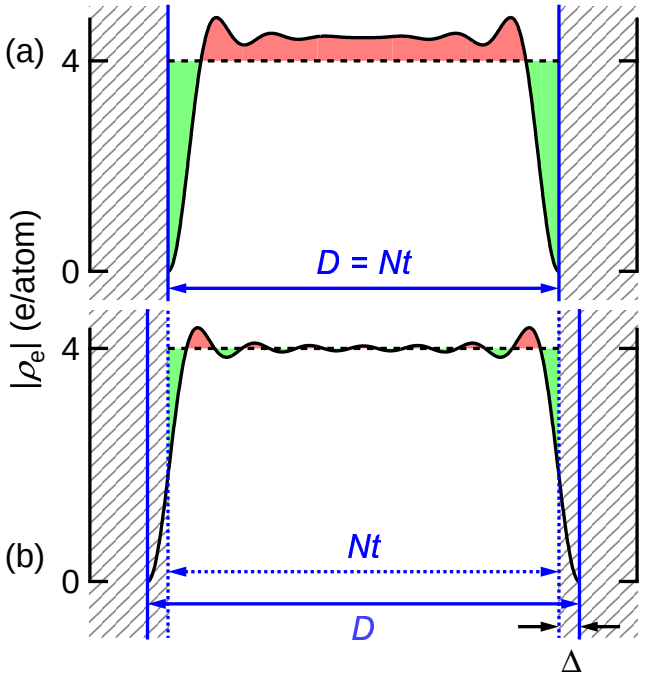

FIG. 3: (Color online) Charge density profiles for a quantum well with $N = 5$. (a) Assuming the boundary potentials are infinite in magnitude, the electronic charge density is forced to zero at the film boundaries, causing an area of electron depletion (shaded areas below $|\rho_e| = 4$, the background charge density from the Pb ion cores). To compensate, the inner portion of the film takes on a net charge. (b) If the charge density is allowed to spill past the classical boundaries of the film, as happens in a real film, this effect can be minimized.

Fermi level must be appropriately chosen so that the film remains electrically neutral overall. The total number of electrons in the film is

$$N_e = N_{\rm val} N \frac{A}{A_{\rm cell}} \tag{17}$$

where $N_{\rm val}$ is the number of itinerant valence electrons per atom of film material ($N_{\rm val} = 4$ for Pb) and $A_{\rm cell}$ is the area of the surface unit cell. The total number of electrons in the theoretical quantum well is calculated by summing over the allowed subbands

$$N_e^{\rm QW} = \frac{V}{2\pi^2 D} \sum_{n=1}^{n_0} \pi \left(k_F^2 - k_z^2\right) \tag{18}$$

$$= \frac{A}{2\pi} C_D \tag{19}$$

where

$$C_D = n_0 k_F^2 - \left(\frac{\pi}{D}\right)^2 \frac{1}{6} n_0 (n_0 + 1)(2n_0 + 1). \tag{20}$$

Setting $N_e^{\rm QW} = N_e$ yields the constraint

$$C_D = \frac{2\pi N_{\rm val} N}{A_{\rm cell}}. \tag{21}$$

The results of solving this constraint for the Fermi energy, $E_F = \frac{\hbar^2 k_F^2}{2m}$, are shown in Fig. 2 (dotted curve) normalized to the bulk free-electron value. As $D \to 0$ the Fermi energy rises steeply and for the first few integer N thicknesses, the Fermi level is up to 40% larger than its bulk value. Cusps are also evident at thicknesses where an additional subband becomes occupied (i.e., when n_0 increases discontinuously) as the film thickness increases.

The steep rise in E_F is specific to the infinite boundary potentials, since it is not present in a finite well model (dashed curve in Fig. 2, see Appendix). The infinite boundary potentials force the wave functions of all the quantum well states to go to zero, creating an area of electron depletion near the film boundaries, as illustrated in Fig. 3(a) with electron density profiles as calculated in Refs. 26 and 47. In order to satisfy the condition of overall charge balance, Eq. (21), the electron density in the center portion of the quantum well must get ever larger with respect to the positive background as the film thickness decreases to compensate for these areas of electron depletion. This charge imbalance leads to a net electric field inside the metal film. However, in a real metal film the confining potentials are not infinite and the electron density will spill slightly past the classical boundaries of the film, reducing the region of electron depletion. To simulate this aspect of the system, define the well width

to be

$$D = Nt + 2\Delta \tag{22}$$

where Δ is the distance the quantum well is allowed to expand at each boundary to allow for some charge spillage. This procedure is analogous to the boundary phase shifts that are often employed in quantum well analyses.[31] For simplicity, we will consider only the symmetric case where the charge spillage at each interface is the same, which is not the case for an actual supported film.[43,47] Therefore, this model should only be considered correct to within an unknown phase shift with respect to the interface. The condition to balance the electron charge density with the positive background of the ion cores near the middle of the metal film can be easily derived and is[47]

$$C_D = \frac{2\pi N_{\rm val} D}{A_{\rm cell} t} - \frac{1}{2}k_F^2. \tag{23}$$

Satisfying this condition minimizes the electric field inside the metal film and hence also its Coulomb energy. Solving Eqs. (21) and (23) simultaneously along with Eq. (22), one finds that the charge spillage is proportional to the Fermi energy

$$\Delta = \frac{A_{\rm cell} t}{4\pi N_{\rm val}} \frac{m}{\hbar^2} E_F. \tag{24}$$

Using the bulk Fermi level for Pb(111) gives a charge spillage of $\Delta = 0.262t$, which is the value that was used in the numerical calculations below. The Fermi level for the infinite well model with this charge spillage is shown in Fig. 2 as a solid curve, which is within 1% of its bulk value for integer $N \geq 1$. Figure 3(b) shows the electronic charge density profile inside the quantum well in this case, where it can be seen that the tails in the density lie partially outside the classical boundaries defined by the positive background, thus reducing the region of electron depletion within the classical boundaries. The result is a surface dipole layer. Note that the issue of charge spillage is automatically accounted for in a model with finite bounding potentials. Such a model is developed in the Appendix, which yields results very similar to the present model.

Using the Fermi level found above for the quantum well with charge spillage, the relative surface energy per surface atom, $E_S = A_{\rm cell}\varepsilon_s$, for a Pb(111) film calculated with Eq. (16) is shown in Fig. 4(a) as a continuous function of N (solid curve). A constant offset, which is irrelevant in a discussion of the relative stability of different thicknesses, has been subtracted off so that the amplitude of the oscillations is more apparent. The oscillations have a wavelength of $\pi/k_F = \lambda_F/2$ (half the Fermi wavelength). This behavior, which is characteristic of quantum size effect phenomena, can be understood as follows. The number of subbands, or Fermi disks (see Fig. 1), that falls below the Fermi level is $n_0 = \text{int}\left(\frac{k_F D}{\pi}\right)$, so every expansion of the well $D \rightarrow D + \pi/k_F$ results in

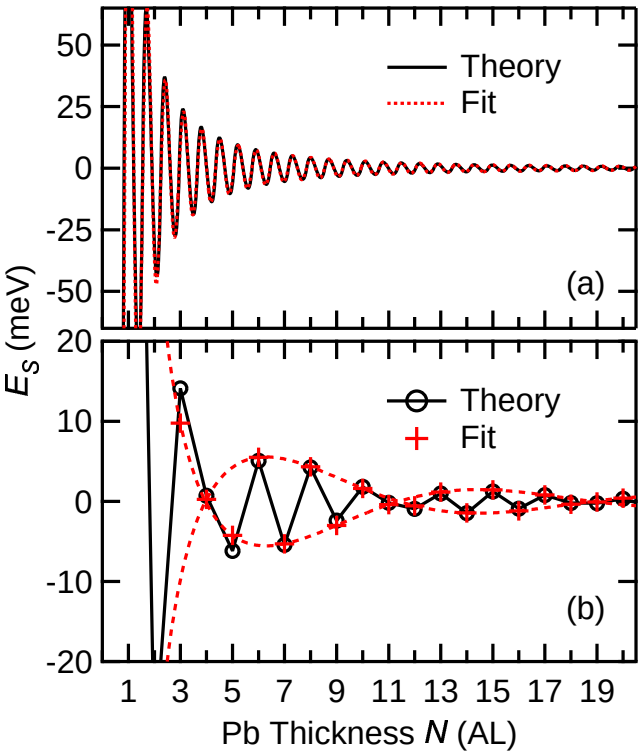

FIG. 4: (Color online) (a) The surface energy for a Pb(111) film calculated using a model based on a free-electron gas confined to an infinite quantum well with charge spillage (solid curve). Oscillations are evident that are well-described by a damped sinusoidal form (dotted curve). (b) The same data for thicknesses of an integer number of atomic layers. Bilayer oscillations within an overlying beating pattern (the envelope for which is shown with dashed curves) result from interference of the oscillations shown in (a) and the discrete lattice of the crystalline film.

an additional subband crossing the Fermi level. This periodic addition of subbands results in oscillations in the surface energy that dampen as the subbands get closer together with increasing film thickness. Since the Fermi level shown in Fig. 2 is relatively constant, the oscillations in the surface energy have a regular periodicity of π/k_F.

Since the film must be composed of an integer number of atomic layers, the surface energy of an actual film will only take on the values at integer N, which are shown in Fig. 4(b) as open circles. Alternations in the values are evident with a phase reversal (even-odd crossover) occurring periodically. This effect is due to interaction of the discrete nature of the atomic lattice structure of the film with the oscillations in the surface energy. Half the Fermi wavelength for Pb(111) is very close to $\frac{2}{3}$ an atomic interlayer spacing; thus, every two film layers corresponds to approximately three full oscillations in the surface energy. Since the relationship is not exact, the bilayer alternations will have a beating pattern superimposed over them causing the phase reversal effect. The

envelope of this beating function is shown in Fig. 4(b) with dashed curves.

The relative surface energy is well-described by the sinusoidal form

$$E_S = A\frac{\sin(2k_F^{\rm bulk}Nt+\phi)}{N^\alpha} + B \qquad (25)$$

where A is an amplitude parameter, ϕ is a phase shift factor that will be dependent on the interface properties of the film, α is a decay exponent, and B is a constant offset, which was subtracted off from E_S to obtain the values in Fig. 4. A fit of this function to the surface energy is shown as a dotted curve in Fig. 4(a) and as crosses in Fig. 4(b). The decay exponent, which is the only parameter value used in the subsequent analysis, was found to be $\alpha = 1.77 \pm 0.09$ over the range of N relevant to this study (it can vary slightly for different ranges of N). This value differs from that used in Ref. 43 due to differences in the model used, which did not take into account charge spillage at the film interfaces. As will be seen in the experimental results, this discrepancy is unimportant.

IV. RESULTS

A. X-ray reflectivity analysis

The samples were grown at 110 K, at which the system is known to follow a metastable layer-by-layer growth mode, allowing films of precise coverage to be grown.[47] Figure 5 shows extended x-ray reflectivity data (points) as a function of $l = q_z a_{\rm Si}\sqrt{3}/(2\pi)$, the perpendicular momentum transfer in Si reciprocal lattice units (1 r.l.u. = 0.668 Å^{-1}), for a sample with a coverage of 6 AL. The reflectivity profiles measured after annealing to the temperatures indicated are shown in progressive order starting from the base temperature at the bottom. Although data were collected every 5–10 K, only select temperatures are shown to illustrate the major morphological changes. The sharp peaks at l = 3, 9, and 12 are the Si(111), (333), and (444) Bragg peaks, respectively, and the interference fringes in-between are due to the Pb overlayers. The broader peaks at $l \approx 3.3$, 6.6, and 9.9 are the Pb(111), (222), and (333) Bragg peaks, respectively. The number and spacing of the fringes between these peaks are an indication of the center of the thickness distribution of the film and its roughness. The reflectivity profiles for smooth films exhibit well-defined fringes with deep minima, similar to an N-slit interference function.[48,51] In such a profile, the number of fringes is equal to the average number of atomic layers in the film minus two. For example, the four well-defined fringes evident between the Pb Bragg peaks in the 110 K data in Fig. 5 are indicative of a smooth film with a thickness of 6 AL. Thus, the appearance of additional fringes at intermediate temperatures indicates that Pb islands with larger thicknesses form on the surface. Detailed analysis of the data indicates that the average island height tends to get larger. That is, the smooth film at 110 K breaks up into nanostructures that get higher with increasing temperature. As discussed below, this curious behavior is related to a tendency for the system to favor the formation of surface regions covered by only a single wetting layer and oscillations in the surface energy similar to those calculated in Sec. III B that favor the formation of islands of specific thicknesses.

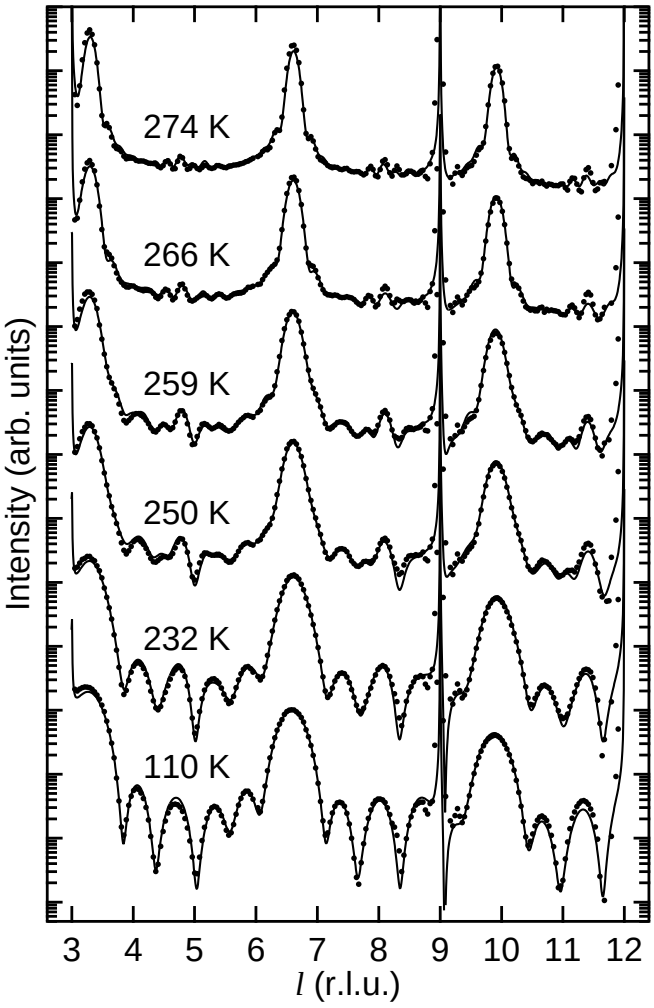

FIG. 5: Extended x-ray reflectivity data (points) for a sample with a coverage of 6 AL after annealing to the temperatures indicated. The sharp peaks at l = 3, 9, and 12 are Bragg peaks from the Si(111) substrate while the fringes in-between are due to the Pb overlayers. Fits using a kinematic model described in the text are shown as solid curves.

The diminished fringes at the highest annealing temperatures indicate a relatively rough film. A broad distribution of thicknesses present on the surface should result in a relatively featureless reflectivity profile in-between the Pb Bragg peaks. However, in this case small oscillations are evident roughly halfway between these peaks. Since these features occur close to the half-order position

for Pb, they are indicative of a bilayer or quasibilayer periodicity in the film structure. Enhanced half-order features due to quasibilayer distortions in the film layer structure have been observed in smooth Pb films.[26,47] However, as is shown below, due to film roughness such lattice distortions do not explain the half-order oscillations in this case. Rather, they can be attributed to a bilayer or quasibilayer periodicity in the thickness distribution $\{p_N\}$.

To illustrate the information content of these near-half-order oscillations and to show this effect is not due to lattice distortions, simulated reflectivity profiles were calculated for various thickness distributions with the atomic layer positions calculated using the model of Refs. 26 and 47, which was found to accurately describe the lattice structure of smooth Pb films. Figure 6(a) shows the reflectivity for a model rough sample with a Gaussian distribution of thicknesses as shown in Fig. 7(a). Even with the presence of quasibilayer lattice distortions, the broad distribution of thicknesses in the film obscures any half-order feature in the curve of Fig. 6(a). However, half-order oscillations are present in the simulated reflectivity of a sample that has a preference for either even or odd thicknesses, as shown in Fig. 6(b) with the distribution used shown in Fig. 7(b). However, the positioning of the oscillations in this case, exactly centered at the half-order position of $l \approx 5$, does not coincide with the positioning of the oscillations in the experimental data shown at the bottom of Fig. 6, as is highlighted with the vertical dotted line. The shifting of the near-half-order oscillations observed can be reproduced by modifying the bilayer distribution of thicknesses so that the preference for even or odd thicknesses switches periodically, as shown in Fig. 7(c). Such an effect is expected due to the beating patterns found in the surface energy in Sec. III B. The corresponding reflectivity for such a simulation is shown in Fig. 6(c), where it can be seen that the near-half-order oscillations are now in phase with those in the data, although they are not reproduced exactly. By letting the p_N be independent parameters and using the values shown in Fig. 7(c) as an initial condition, an accurate fit to the data can be obtained, the results of which are shown in Fig. 7(d). Thus, the presence of the near-half-order oscillations in the data and their position relative to the Pb Bragg peaks is indicative of quasibilayer oscillations in the surface energy as a function of thickness.

Detailed information on the surface morphology was obtained by fitting each reflectivity profile using the kinematic model from Sec. III A to obtain the thickness distribution present on the surface, $\{p_N\}$. Each p_N parameter was ultimately fit as an independent parameter except for p_1, the coverage of the wetting layer, which was constrained such that Eq. (4) was satisfied. At the higher annealing temperatures, when the distribution of thicknesses present on the surface is broad, the number of non-zero p_N values needed to describe the surface morphology is large. Local minima in parameter space were avoided by starting the fit for each temperature (except the first) from the best fit of the previous temperature, effectively following the film morphology as it evolves. Due to the large number of independent parameters used in some of the fits, the sensitivity of the fits to any individual p_N value was weak; however, as demonstrated with Figs. 6 and 7, the overall distribution of p_N values is well-determined by the information contained in the near-half-order oscillations in the x-ray reflectivity profiles. As a consequence, given the confidence in the form of the thickness distribution demonstrated above, we estimate the relative errors to be within 10% of each p_N value. The partial coherence factor in Eq. (8) was found

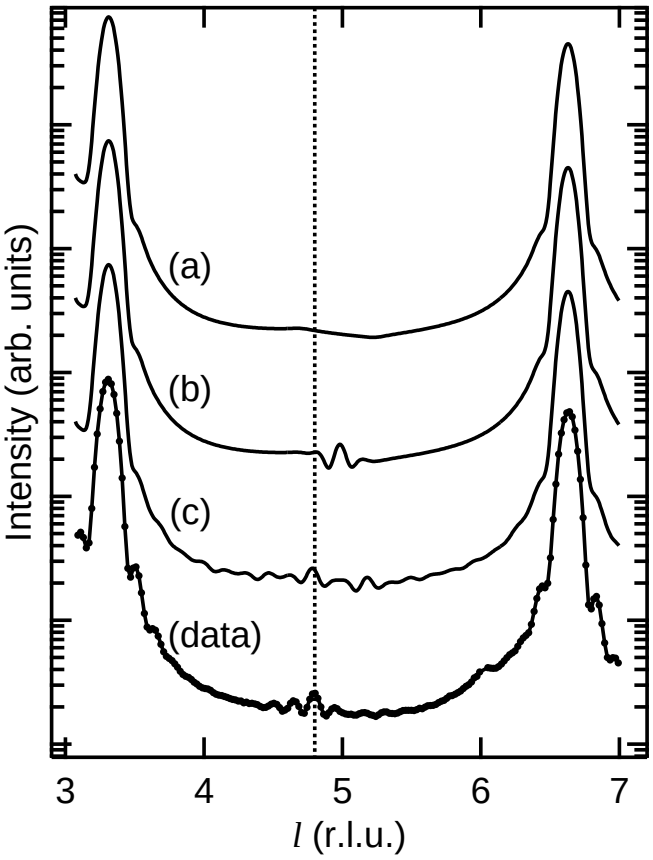

FIG. 6: Simulations showing that the near-half-order oscillations in the reflectivity of samples annealed to high temperatures contain a significant amount of information. The corresponding thickness distributions are shown in Fig. 7. (a) The reflectivity from a surface whose thickness distribution follows a simple Gaussian. There are no oscillations in the reflectivity near the half-order point for the film overlayers. (b) A bilayer preference is added to the thickness distribution which results in oscillations centered at the half-order point, $l \approx 5$. (c) Phase reversal (even-odd crossover) is added to the bilayer distribution with the periodicity expected (every 9 AL). The oscillations are shifted slightly from the exact half-order position, coinciding more with those in the experimental data shown at the bottom, as highlighted with the vertical dotted line.

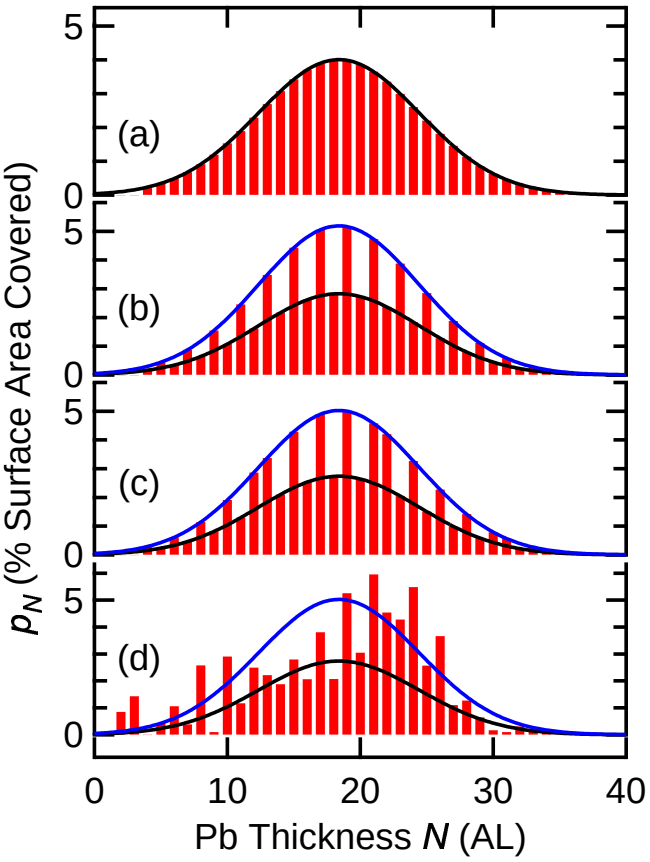

FIG. 7: (Color online) The thickness distributions used in the simulations of Fig. 6. (a) A simple Gaussian distribution. (b) A dual-Gaussian distribution where the upper envelope dictates the values for odd N. (c) The same dual-Gaussian distribution with an even-odd crossover every 9 AL, the expected period of the beating function in the surface energy with the empirical Fermi wavelength. (d) The distribution resulting from a fit to the experimental data at the bottom of Fig. 6, starting from the distribution in (c). In all cases, the coverage of the film overlayers, Eq. (5), is constrained to 11 AL (the coverage of the film whose data is shown) and the wetting layer, p_1, was adjusted such that the surface formed a closed film [Eq. (4)].

to be near unity (all coherent scattering) for the lower annealing temperatures and on the order of 0.5 for the highest temperatures.

B. Evolution of film morphology with annealing

The thickness distributions determined from the fits to the reflectivity data in Fig. 5 are shown in Fig. 8. After deposition at 110 K, the thickness distribution is sharply peaked about $N = 6$, corresponding to a very smooth film with a root-mean-square (rms) roughness of about 1.3 Å. Upon annealing, no discernable changes in the reflectivity profile are observed until 232 K, at which point regions of 8 and 10 AL start to form. These regions then become more prevalent by 250 K and the residual 7 AL region has disappeared, which is a less-stable thickness. The dominant thickness of the film is still 6 AL up to 266 K, though, at which point the distribution has broadened significantly. At 274 K, the preference for 6 AL due to the initial condition has disappeared and the surface has presumably reached a state of local equilibrium in which each thickness N is in equilibrium with its neighboring thicknesses $N \pm 1$. The rms roughness at this temperature is about 18 Å. The thickness distributions show a clear preference for certain thicknesses over others with a quasibilayer periodicity, which we expect because of the near-half-order oscillations present in the reflectivity profiles of Fig. 5, as discussed above. Two of the expected crossover points are evident as well at $N \approx 5$ and $N \approx 14$.

Phenomenologically, the fact that the thickness distribution gets broader after annealing is actually expected when one considers that the system follows a Stranski-Krastanov growth mode at room temperature, where islands form on top of a single wetting layer. However, in this case the distribution of thicknesses not only broadens, but its center moves upwards in N. That is, at lower temperatures, the distributions in Fig. 8 are peaked about the initial thickness of 6 AL, but at the final temperature, the average structure height above the wetting layer is about 12 AL, which implies that on average the surface features are getting higher with increasing temperature. To conserve the amount of Pb on the surface, the initially smooth film must break up into islands separated by increasingly wide regions of the surface covered only by a wetting layer. The amount of the surface covered by only a wetting layer, p_1, found in our analysis is shown in Fig. 9. It increases monotonically with the annealing temperature. The most stable configuration of the system is to maximize the coverage of the wetting layer, which is supported by first-principles calculations that show a deep global minimum at $N = 1$ in the surface energy.[42] However, the system cannot fully maximize the coverage of the bare wetting layer due to kinetic limitations and thermal fluctuations that will tend to roughen the surface and favor a reasonable nanostructure height. The combination of these effects explains the annealing behavior observed.

In contrast to the 6 AL film, whose initial thickness persisted through most of the annealing process, indicating that this thickness is preferred, films with initial thicknesses that are not preferred exhibit a qualitatively distinct behavior. Figure 10 shows the thickness distributions for a film with a coverage of 11 AL and its morphological changes upon annealing to the indicated temperatures. As with the 6 AL film, the initial distribution is sharply peaked about the initial thickness, consistent with a layer-by-layer growth mode. However, in this case the initially smooth film (3.2 Å rms roughness) begins to break up at a much lower temperature of 174 K. By 200 K, the coverage of the initial 11 AL has largely disappeared and the film has bifurcated into the neighboring

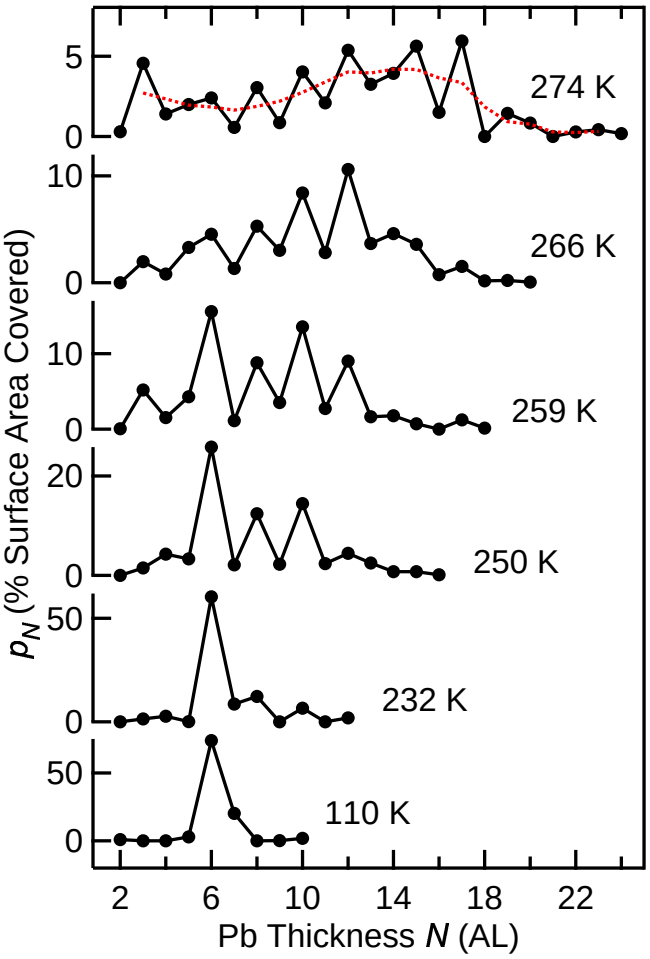

FIG. 8: (Color online) The coverage of different thicknesses present on the sample surface for each corresponding curve in Fig. 5, with the annealing temperatures indicated. The coverage values were determined via a fit using a model described in the text. The surface evolution is shown to progress from a very smooth film at 110 K through various metastable "preferred thickness" states before reaching a state of local equilibrium. The preference of certain thicknesses over others corresponds to quasibilayer oscillations in the surface energy. The dotted line through the 274 K data is the result of applying a binomial filtering algorithm to the values for an analysis of the surface energy.

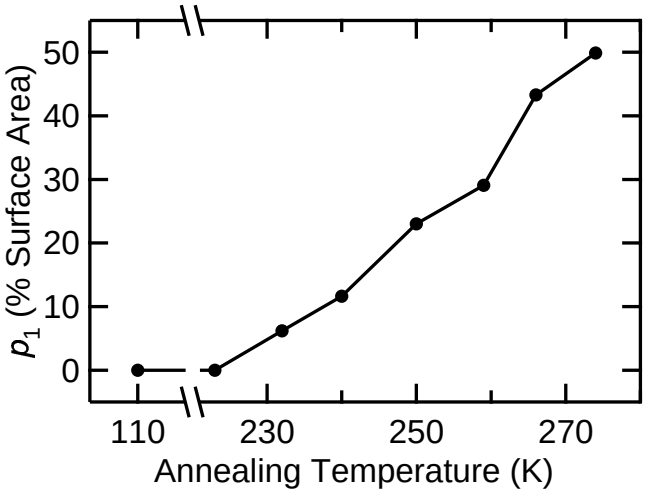

FIG. 9: The amount of the sample surface covered only by a single wetting layer increases with temperature. The surface energy has a deep global minimum at $N = 1$ that results in the wetting layer being the most stable configuration of the system.

thicknesses of 10 and 12 AL, both of which are more stable than 11 AL. At 253 K, the surface is dominated by regions of 12 AL, resulting from phase separation of the system into a state corresponding to a local minimum in the surface energy at $N = 12$ and a state in the global minimum at $N = 1$. It is this temperature range in which uniform-height nanomesas have been observed in many other studies.[17–19,21–23,42] Annealing to higher temperatures results in a broadening of the thickness distribution until at 280 K, when the residual preference for 12 AL from the uniform-height phase has disappeared, the film has reached local equilibrium (28 Å rms roughness). Since we started with a thicker film, there are more Pb atoms to rearrange and nanostructures of larger height are able to form on the surface. The final distribution of thicknesses is correspondingly much broader and has a higher average structure height above the wetting layer of approximately 18 AL. As a result, the oscillations in the distribution, which are indicative of variations in the relative stability of different thicknesses, are present over a wider range, allowing a more comprehensive analysis of the surface energy.

C. Surface energy

The variations in the thickness distributions of Figs. 8 and 10 are indicative of a relative preference for certain thicknesses over others. An experimental measure of the relative stability of a thickness can be obtained by comparing the fractional surface area it covers with that of its neighbors

$$p_N - \frac{p_{N-1} + p_{N+1}}{2} = -\frac{1}{2} p''_N \qquad (26)$$

where p''_N is the discrete second derivative of p_N. That is, thicknesses for which the local curvature of p_N is negative ($p''_N < 0$) are relatively stable, since they cover more of the sample surface compared with their neighboring thicknesses. Conversely, if the local curvature of p_N is positive ($p''_N > 0$), the thickness N is relatively unstable since the system prefers to form regions with thicknesses of $N \pm 1$. The values of p''_N for the highest annealing temperature data in Figs. 8 and 10 are shown as solid circles in Figs. 11(a) and 11(b), respectively. In both cases, quasibilayer oscillations about $p''_N = 0$ are evident, a reflection of variations in the relative stability of different thicknesses. As mentioned above, the 11 AL sample

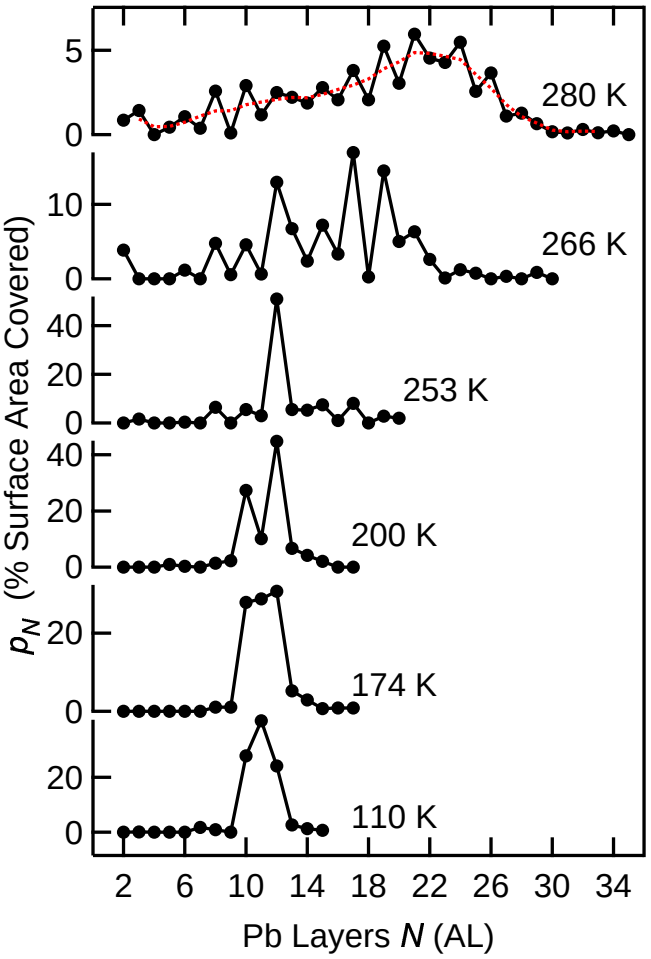

FIG. 10: (Color online) Evolution of the morphology of an 11 AL film after annealing to the temperatures indicated. In contrast to the 6 AL film, which is a more stable thickness, this film bifurcates at the comparatively low temperature of 174 K. Due to the higher volume (coverage) of Pb in the film, the final distribution of thicknesses is broader and peaked at a greater thickness than that in Fig. 8, providing information about the surface energy over a broader range of thicknesses.

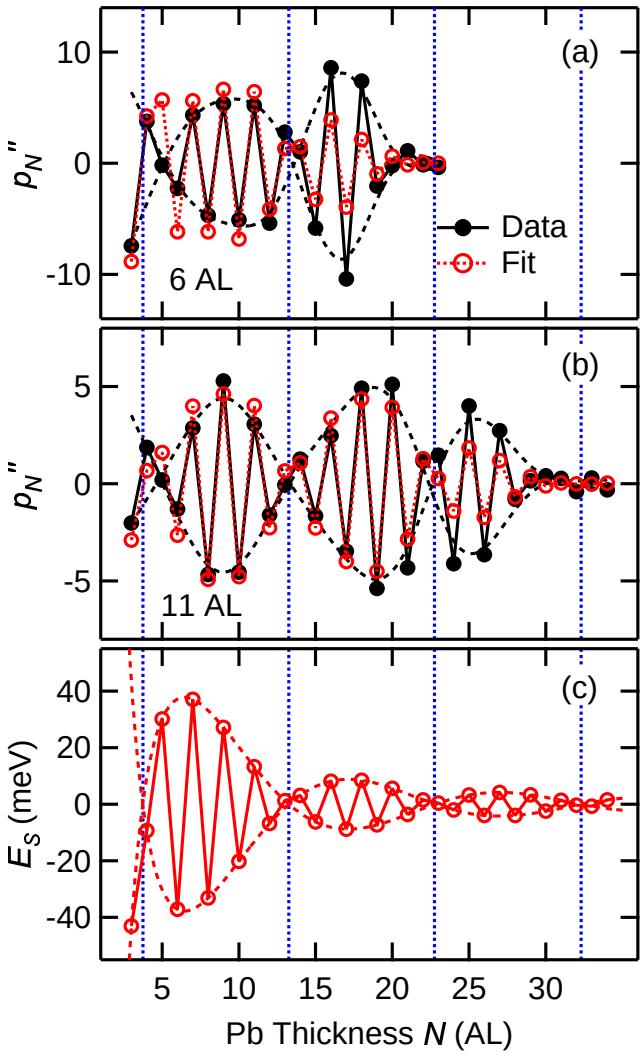

FIG. 11: (Color online) The discrete second derivative of the p_N values for the 274 K and 280 K data in Figs. 8 and 10 are shown as solid circles in (a) and (b), respectively. Two-parameter fits to these data as described in the text are shown as open circles, which accurately reproduce the quasibilayer oscillations and envelope beating function. (c) The surface energy as calculated using Eq. (25) with the average parameters from the two fits in (a) and (b). Dashed lines show the beating envelopes for the experimental values in (a) and (b) and the calculated values in (c). Vertical dotted lines indicate the nodes in the beating envelope of the surface energy in (c), which correspond closely to the nodes in (a) and (b).

provides information over a wider range of thicknesses than the 6 AL sample due to its greater initial thickness.

This effect will manifest itself as corresponding variations in the surface energy, similar to those seen in the free-electron calculations of Sec. III B. We can extract empirical information about the surface energy by relating it to the p_N parameters, which should follow a Boltzmann distribution

$$p_N = \mathcal{X} e^{-E_S(N)/k_B T} \tag{27}$$

where k_B is Boltzmann's constant and T is taken to be the annealing temperature. In the case of a system that is in global thermodynamic equilibrium, $\mathcal{X}$ is simply a constant of proportionality. However, in the present case we only assume that the system is in a state of local equilibrium, in which case $\mathcal{X}$ is a slowly varying function of N. Thus, $\mathcal{X}$ will depend on a variety of factors, including the film's annealing history. To remove this ill-defined function from the analysis, we consider instead the self-normalized local variations in p_N

$$\delta p_N \equiv \frac{p_N - \overline{p}_N}{\overline{p}_N}, \tag{28}$$

where $\overline{p}_N$ is a local average of p_N. Such a quantity corresponds to the smoothly varying background underlying the oscillations in the p_N values of Figs. 8 and 10. As long as $\overline{p}_N$ is calculated using only a small local set of p_N

values, we can regard $\mathcal{X}$ as being approximately constant over this set and δp_N is independent of $\mathcal{X}$. A reasonable method for calculating the local average is to use a binomial filtering algorithm[53]

$$\overline{p}_N = \frac{p_{N-1} + 2p_N + p_{N+1}}{4}. \tag{29}$$

The $\overline{p}_N$ values resulting from the application of this algorithm to the top p_N distributions in Figs. 8 and 10 are shown as dotted curves, which show that it indeed produces smooth curves. Using this algorithm also has the additional benefit that δp_N is simply related to the discrete second derivative of p_N

$$\delta p_N = \frac{-p''_N}{4\overline{p}_N}. \tag{30}$$

The empirical discrete second derivative values in Figs. 11(a) and 11(b) were fit using the function

$$(p''_N)_{\text{theory}} = -4\,(\overline{p}_N)_{\text{expt}}\,(\delta p_N)_{\text{theory}}\,, \tag{31}$$

where the theoretical version of δp_N is

$$(\delta p_N)_{\text{theory}} = \frac{4p_N}{p_{N-1} + 2p_N + p_{N+1}} - 1, \tag{32}$$

with the p_N values calculated using Eq. (27) and the sinusoidal approximation for the surface energy found from the free-electron model calculation, Eq. (25). Note that when this form for E_S is used, the constant offset in Eq. (25), B, cancels from Eq. (32). Due to a significant covariance found between the parameters A and α, where the adjustment of one parameter could be largely compensated for by a complementary adjustment of the other, the value for the decay exponent found in Sec. III B, $\alpha = 1.77$, was fixed in the fits. In Ref. 43 an exponent value of $\alpha = 0.938$ was used for which similarly accurate fits were obtained. The analysis was thus found to be relatively insensitive to the specific value of the decay exponent, as long as it was between $0.9 < \alpha < 2.0$ and the surface energies found in the two results differ by less than 3 meV for most of the thickness range available. The Fermi wave vector was taken to be the empirical value for bulk Pb(111), $k_F = 1.59$ Å^{-1}. Thus, only two adjustable parameters were used in the fits: A and ϕ. The fitted value of ϕ was $(0.49 \pm 0.01)\pi$ for both fits and the fitted value of A was 1.0 ± 0.3 eV for the 6 AL sample and 1.3 ± 0.2 eV for the 11 AL sample. The surface energy shown in Fig. 11(c) was calculated using the average of these two values.

D. Discussion

The annealing behavior of the two films is consistent with the surface energy shown in Fig. 11(c). At low temperatures, the system is kinetically limited and can therefore be found in a metastable state where the predominant thickness is energetically unfavorable, as with the 11 AL film in this study. However, as the film is annealed and given more thermal energy, the unstable 11 AL thickness easily bifurcates into the energetically preferred thicknesses of 10 and 12 AL. Upon further annealing, in some cases the film coalesces into a state where the surface is mostly covered by islands of uniform height. For the initial 11 AL film, the preferred thickness of the islands (nanomesas) is 12 AL, which is actually indicated to have a higher surface energy than 10 AL in Fig. 11(c). However, the system is prevented from forming uniform 10 AL islands since this thickness is smaller than the initial thickness, and the deep minimum in the surface energy for $N = 1$ favors the formation of surface regions covered only by a single wetting layer. As a consequence, a state that consists in 12 AL islands separated by regions of the surface covered only by the wetting layer is favored over a state in which both 10 and 12 AL islands are present.

In contrast, for a film whose initial predominant thickness is more stable, like the 6 AL film in this study, the surface morphology remains unchanged up to a much higher temperature. When it does begin to evolve, the initial 6 AL portion of the film is mostly retained while the unstable thicknesses (e.g., 7 AL) transform into higher stable thicknesses. The coverage of the initial thickness in this case only slowly decays with increasing temperature until local equilibrium is attained. We have collected similar data for other initial thicknesses, both preferred and not preferred, the annealing behavior of which is consistent with the results presented here.

The overall phase shift of the surface energy and its envelope beating function depends only on the boundary conditions at the film interfaces. As such, the nodal points in the surface energy envelope (the points where even-odd crossover occurs) should be found in the same places for the two data sets, which is indeed the case as seen in Fig. 11. Due to the idealized boundary conditions used in the free-electron model of Sec. III B, the phase shift in the surface energy calculated from it is different from the experimentally determined phase shift, as one would expect. The amplitudes of oscillation found experimentally are consistent with the amplitude found in first-principles calculations[37,42] and the nodes in the beating envelope occur with the periodicity expected given the bulk Fermi energy, although there is a slight discrepancy for the first node at $N \approx 5$. In this thickness region, interface effects are more significant and the free-electron approximation of the surface energy, Eq. (25), becomes less accurate. However, the empirical stability data for the lower N values in Figs. 11(a) and (b) is supported by independent photoemission measurements,[38] indicating that the data is reliable.

V. SUMMARY

We have presented temperature-dependent x-ray diffraction data showing the morphological evolution of

Pb films grown on Si(111) substrates. The films were grown at 110 K, at which temperature the system follows a metastable layer-by-layer growth mode. By annealing the films to around 280 K in increments of 5–10 K, the surface morphology was observed passing through various metastable states before reaching a roughened state characterized by local equilibrium. The annealing behavior of two films with different initial thicknesses clearly shows that certain film thicknesses are more stable than others. A film with an initial thickness that is relatively stable (6 AL) remained intact up until approximately 230 K, at which point it began to roughen and explore the broader energy landscape. In contrast, a film with an initial thickness that is relatively unstable (11 AL) began to break up at the comparatively low temperature of 170–200 K, at which point it decomposed (phase separated) into regions of thicknesses with lower surface energies (islands dominated by a single height, 12 AL, surrounded by regions covered by the wetting layer only). This phenomenon of preferred heights can be explained by the phase separation of the system into a state corresponding to a local minimum in the surface energy (the uniform-height islands) and a state in the global minimum (the wetting layer).

A model based on a free-electron gas confined to an infinite quantum well, with charge spillage accounted for, was derived that shows quasibilayer oscillations in the surface energy consistent with the morphologies observed in the experiments. The oscillations in the free-electron surface energy are found to closely follow a damped sinusoidal form with a wavelength of $\lambda_F/2$. This result is used to relate the details of the broad thickness distributions of the annealed films to their surface energy. These results draw a direct link between the formation of quantized electronic states due to confinement of the itinerant electrons to a metal film and the relative stability of different film thicknesses, which can exhibit large variations for sizes differing by as little as a single atomic layer. Understanding such effects is critical for the engineering of metallic nanoscale devices.

Acknowledgments

This work is based upon work supported by the U.S. Department of Energy, Division of Materials Sciences (Grant No. DEFG02-91ER45439). The UNICAT facility at the Advanced Photon Source (APS) is supported by the U.S. Department of Energy through the Frederick Seitz Materials Research Laboratory at the University of Illinois at Urbana-Champaign, the Oak Ridge National Laboratory, the National Institute of Standards and Technology, and UOP LLC. The APS is supported by the U.S. Department of Energy (Grant No. W-31-109-ENG-38). We also acknowledge partial equipment and personnel support from the Petroleum Research Fund, administered by the American Chemical Society, and the U.S. National Science Foundation (Grant No. DMR-02-03003).

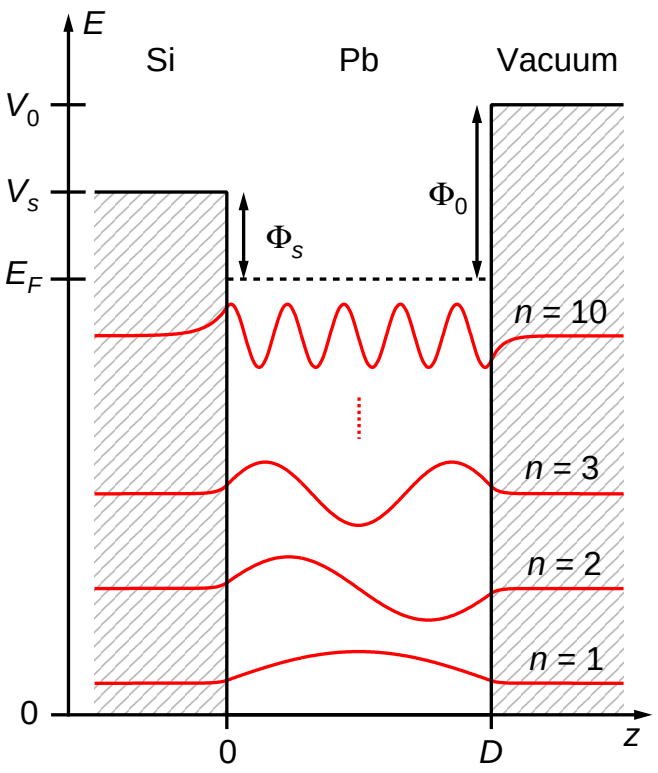

FIG. 12: (Color online) A schematic of the finite quantum well used to calculate the surface energy. Two potential barriers confine the quantum well states to the Pb film in the middle of the diagram. The wave functions are shown for $n = 1$, 2, 3, and 10.

APPENDIX

An alternative model for the surface energy of a thin metal film to the one presented in Sec. III B can be constructed with finite potential barriers. The quantum well for such a model is shown schematically in Fig. 12, where V_s is the confining potential at the buried interface, and V_0 is the vacuum confinement potential. These potentials can be broken up into the components

$$\begin{aligned} V_s &= E_F + \Phi_s \\ V_0 &= E_F + \Phi_0 \end{aligned} \tag{A.1}$$

where Φ_0 is the work function of the film material and Φ_s is an effective potential step encountered by an electron travelling between the film and substrate. In an actual physical system, the electrons in the film material are confined by the band gap of the semiconductor substrate, which does not behave like a simple potential barrier.[31] Thus, a simple step-potential model is not expected to accurately describe the system. Nonetheless, the finite quantum well model provides an alternative to the infinite well and illustrates some of the general strengths

and weaknesses of using a free-electron model. In all subsequent calculations, we will use the values $\Phi_0 = 4$ eV, the work function of Pb, and $\Phi_s = 0.6$ eV, the Schottky barrier of the Pb/Si(111) interface.[54]

The z components of the wave functions for the confined states in this model are of the form

$$\psi(z) = \begin{cases} C_1 \exp(\kappa_s z) & z < 0 \\ C_2 \sin(k_z z) + C_3 \cos(k_z z) & 0 < z < D \\ C_4 \exp[-\kappa_0 (z - D)] & z > D \end{cases} \quad \text{(A.2)}$$

where C_1–C_4 are constants subject to normalization and boundary conditions and κ_s, κ_0, and k_z are all real quantities for confined states. Enforcing energy conservation among the three separate regions yields the relations

$$\begin{aligned} \kappa_s &= \sqrt{\frac{2mV_s}{\hbar^2} - k_z^2} \\ \kappa_0 &= \sqrt{\frac{2mV_0}{\hbar^2} - k_z^2}. \end{aligned} \quad \text{(A.3)}$$

and requiring continuity of $\psi(z)$ and its first derivative at the well boundaries results in the transcendental equation

$$\tan(k_z D) = \frac{\kappa_s + \kappa_0}{k_z^2 - \kappa_s \kappa_0} k_z. \quad \text{(A.4)}$$

Due to the periodic nature of the tangent function on the left side of this equation, there will be a series of discrete solutions to this equation for k_z (and thus also κ_s and κ_0) corresponding to the wave functions for the different possible subbands shown in Fig. 1. Specifically, using the trigonometric identity

$$\arctan\left(\frac{x + y}{1 - xy}\right) = \arctan x + \arctan y \quad \text{(A.5)}$$

Eq. (A.4) can be rewritten as

$$k_z D = n\pi - \arctan\left(\frac{k_z}{\kappa_s}\right) - \arctan\left(\frac{k_z}{\kappa_0}\right), \quad \text{(A.6)}$$

where the integer n is the subband quantum number. Note that in the limit $V_s, V_0 \to \infty$, this equation reduces to Eq. (10), the quantization condition for the infinite well. Equation (A.6) is the usual Bohr-Sommerfeld quantization rule, with the two arctangent terms related to the phase shifts at the two boundaries. Sample wave functions for different solutions are shown in Fig. 12. In this case, the quantum number of the highest occupied subband must be found numerically.

As in Sec. III B, the Fermi level must be appropriately chosen so that the number of electrons in the quantum well, Eq. (18), remains equal to the number of free electrons given the amount of film material, Eq. (17). The resulting Fermi level for a Pb(111) film is shown in Fig. 2 as a dashed curve, which is very similar to that found in the infinite well model with charge spillage. In this case, the Fermi energy remains above the bulk value for all

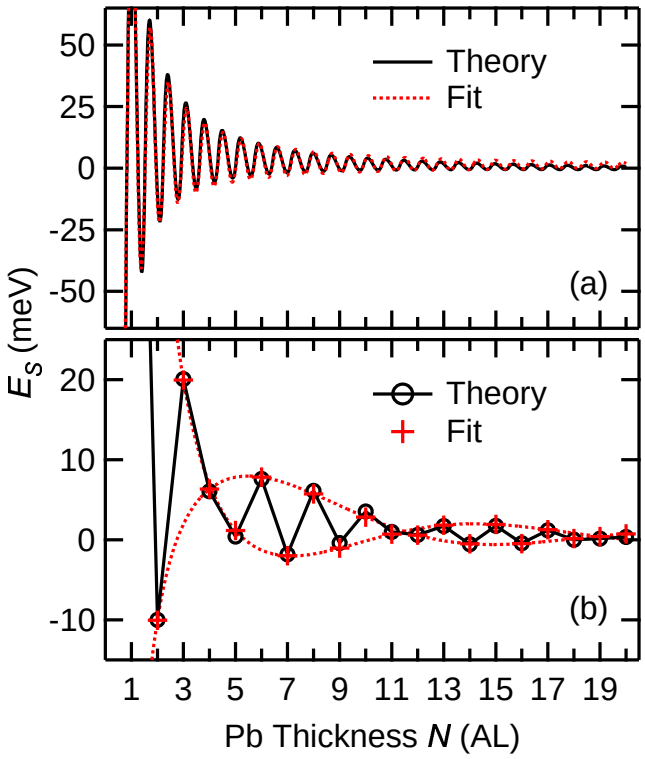

FIG. 13: (Color online) (a) The surface energy for a Pb(111) film calculated using a model based on a free-electron gas confined to a finite quantum well (solid curve), along with a fit to a damped sinusoidal function (dotted curve). (b) The same data for integer numbers of atomic layers. Bilayer oscillations similar to those in Fig. 4(b) are evident.

thicknesses, though, with its value about 4% larger than the bulk for $N = 1$ and much closer thereafter.

A completely analogous procedure can be used to reach Eq. (12) for the total electronic energy of the film and

$$\varepsilon_s = \frac{\hbar^2}{16\pi m}\left[\sum_{k_z < k_F}\left(k_F^4 - k_z^4\right) - \frac{4}{5\pi}\left(k_F^{\text{bulk}}\right)^5 D\right] \quad \text{(A.7)}$$

for the surface energy density. The relative surface energy per surface atom is shown in Fig. 13(a) with the values for integer N shown in Fig. 13(b). It exhibits oscillations similar to those seen with the infinite well in Fig. 4. A slight upwards bend to the surface energy is apparent as $N \to 0$, which is particularly noticeable in the integer N data of Fig. 13(b). This effect can be accounted for by adding an additional parameter to Eq. (25)

$$E_S = A\frac{\sin(2k_F^{\text{bulk}} N t + \phi) + C}{N^\alpha} + B. \quad \text{(A.8)}$$

A fit to the surface energy with this equation is shown in Fig. 13(a) with a dotted curve and Fig. 13(b) with crosses. The decay exponent in this case was found to be $\alpha = 1.74 \pm 0.05$, consistent with the decay exponent of the infinite well model. The amplitude was also found

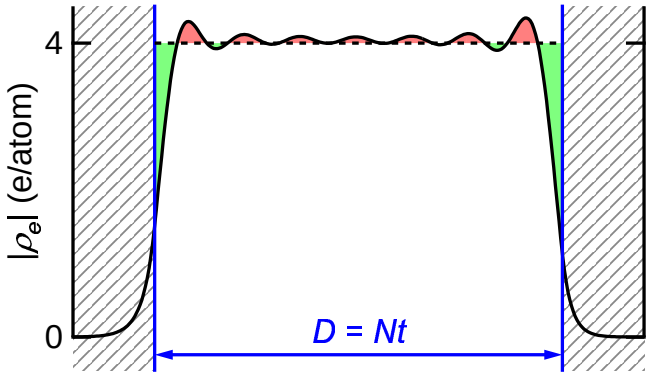

FIG. 14: (Color online) The electronic charge density inside the film calculated with the finite well model. The profile is very similar to that from the infinite well model with charge spillage, Fig. 3(b). However, the average density inside the film does not exactly cancel with the positive ionic background, resulting in the upwards bend in the surface energy as $N \to 0$.

to be similar. Both models exhibit quasibilayer oscillations that decay as $\sim N^{-1.75}$ with thickness, which is the primary result taken from the free-electron calculations. The extra parameter C in Eq. (A.8) was found to be unimportant in our fit to the experimental data and is therefore not used.

The charge density inside the finite well can be calculated in the same manner as for an infinite well.[26,47] The full wave function is this case is

$$\Psi_{\mathbf{k}}(\mathbf{r}) = \frac{1}{\sqrt{A}} e^{ik_x x + ik_y y} \psi_n(z) \tag{A.9}$$

and the electronic charge density as a function of z is

$$\rho_e(z) = -\frac{e}{2\pi} \sum_{k_z < k_F} \left(k_F^2 - k_z^2\right) \left|\psi_n(z)\right|^2. \tag{A.10}$$

A plot of the electron density for $N = 5$ is shown in Fig. 14. As one would expect, the electron density spills past the classical boundaries of the film due to the finite potential barriers, similar to the curve in Fig. 3(b). However, we have not imposed any condition of charge balance analogous to that done for the infinite well model with Eq. (23). Since the charge spillage is automatically accounted for in this model, we do not have an additional parameter such as the Δ used in the infinite well model that can be adjusted to meet such a constraint. As a result, the oscillations in the electron density inside the film do not exactly cancel with the positive background from the ion cores and a net electric field is present in the film. This situation is similar to that in Fig. 3(a), but to a much lesser degree. In that case, the charge imbalance in the quantum well resulted in a substantial upwards bend in the Fermi level as $N \to 0$, which translates into a similar effect in the surface energy.

* Electronic address: chiang@mrl.uiuc.edu

1 F. K. Schulte, Surf. Sci. **55**, 427 (1976).
2 S. Ciraci and I. P. Batra, Phys. Rev. B **33**, 4294 (1986).
3 P. J. Feibelman, Phys. Rev. B **27**, 1991 (1983).
4 G. A. Sorokin, Sov. Phys. Solid State **15**, 1231 (1973).
5 J. M. Blatt and C. J. Thompson, Phys. Rev. Lett. **10**, 332 (1963).
6 B. G. Orr, H. M. Jaeger, and A. M. Goldman, Phys. Rev. Lett. **53**, 2046 (1984).
7 Y. Guo, Y.-F. Zhang, X.-Y. Bao, T.-Z. Han, Z. Tang, L.-X. Zhang, W.-G. Zhu, E. G. Wang, Q. Niu, Z. Q. Qiu, et al., Science **306**, 1915 (2004).
8 T.-C. Chiang, Science **306**, 1900 (2004).
9 N. Trivedi and N. W. Ashcroft, Phys. Rev. B **38**, 12298 (1988).
10 I. Vilfan, M. Henzler, O. Pfennigstorf, and H. Pfnür, Phys. Rev. B **66**, 241306 (2002).
11 P. Saalfrank, Surf. Sci. **274**, 449 (1992).
12 I. B. Altfeder, K. A. Matveev, and D. M. Chen, Phys. Rev. Lett. **78**, 2815 (1997).
13 J. Braun and J. P. Toennies, Surf. Sci. **384**, L858 (1997).
14 L. Gavioli, K. R. Kimberlin, M. C. Tringides, J. F. Wendelken, and Z. Zhang, Phys. Rev. Lett. **82**, 129 (1999).
15 J. J. Paggel, C. M. Wei, M. Y. Chou, D.-A. Luh, T. Miller, and T.-C. Chiang, Phys. Rev. B **66**, 233403 (2002).
16 P. J. Feibelman and D. R. Hamann, Phys. Rev. B **29**, 6463 (1984).
17 K. Budde, E. Abram, V. Yeh, and M. C. Tringides, Phys. Rev. B **61**, R10602 (2000).
18 V. Yeh, L. Berbil-Bautista, C. Z. Wang, K. M. Ho, and M. C. Tringides, Phys. Rev. Lett. **85**, 5158 (2000).
19 W. B. Su, S. H. Chang, W. B. Jian, C. S. Chang, L. J. Chen, and T. T. Tsong, Phys. Rev. Lett. **86**, 5116 (2001).
20 W.-B. Su, S.-H. Chang, C.-S. Chang, L. J. Chen, and T. T. Tsong, Jap. J. Appl. Phys. **40**, 4299 (2001).
21 M. Hupalo, S. Kremmer, V. Yeh, L. Berbil-Bautista, E. Abram, and M. C. Tringides, Surf. Sci. **493**, 526 (2001).
22 M. Hupalo, V. Yeh, L. Berbil-Bautista, S. Kremmer, E. Abram, and M. C. Tringides, Phys. Rev. B **64**, 155307 (2001).
23 M. Hupalo and M. C. Tringides, Phys. Rev. B **65**, 115406 (2002).
24 B. J. Hinch, C. Koziol, J. P. Toennies, and G. Zhang, Vacuum **42**, 309 (1991).
25 L. Huang, S. J. Chey, and J. H. Weaver, Surf. Sci. **416**, L1101 (1998).
26 P. Czoschke, H. Hong, L. Basile, and T.-C. Chiang, Phys. Rev. Lett. **91**, 226801 (2003).
27 M. Valden, X. Lai, and D. W. Goodman, Science **281**, 1647 (1998).
28 N. D. Lang and W. Kohn, Phys. Rev. B **1**, 4555 (1970).
29 Z. Zhang, Q. Niu, and C.-K. Shih, Phys. Rev. Lett. **80**, 5381 (1998).
30 T. Valla, M. Kralj, A. Šiber, M. Milun, P. Pervan, P. D. Johnson, and D. P. Woodruff, J. Phys.: Condens. Matter **12**, L477 (2000).

[31] T.-C. Chiang, Surf. Sci. Rep. **39**, 181 (2000).
[32] L. Aballe, A. Barinov, A. Locatelli, S. Heun, and M. Kiskinova, Phys. Rev. Lett. **93**, 196103 (2004).
[33] D.-A. Luh, T. Miller, J. J. Paggel, and T.-C. Chiang, Phys. Rev. Lett. **88**, 256802 (2002).
[34] G. Materzanini, P. Saalfrank, and P. J. D. Lindan, Phys. Rev. B **63**, 235405 (2001).
[35] R. Otero, A. L. Vázquez de Parga, and R. Miranda, Phys. Rev. B **66**, 115401 (2002).
[36] D. Schmicker, T. Hibma, K. A. Edwards, P. B. Howes, J. E. Macdonald, M. A. James, M. Breeman, and G. T. Barkema, J. Phys.: Condens. Matter **9**, 969 (1997).
[37] C. M. Wei and M. Y. Chou, Phys. Rev. B **66**, 233408 (2002).
[38] M. H. Upton, C. M. Wei, M. Y. Chou, T. Miller, and T.-C. Chiang, Phys. Rev. Lett. **93**, 026802 (2004).
[39] J.-H. Cho, K. S. Kim, C. T. Chan, and Z. Zhang, Phys. Rev. B **63**, 113408 (2001).
[40] C. M. Wei and M. Y. Chou, Phys. Rev. B **68**, 125406 (2003).
[41] D.-A. Luh, T. Miller, J. J. Paggel, M. Y. Chou, and T.-C. Chiang, Science **292**, 1131 (2001).
[42] H. Hong, C.-M. Wei, M. Y. Chou, Z. Wu, L. Basile, H. Chen, M. Holt, and T.-C. Chiang, Phys. Rev. Lett. **90**, 076104 (2003).
[43] P. Czoschke, H. Hong, L. Basile, and T.-C. Chiang, Phys. Rev. Lett. **93**, 036103 (2004).
[44] W. B. Jian, W. B. Su, C. S. Chang, and T. T. Tsong, Phys. Rev. Lett. **90**, 196603 (2003).
[45] A. Mans, J. H. Dil, A. R. H. F. Ettema, and H. H. Weitering, Phys. Rev. B **66**, 195410 (2002).
[46] M. H. Upton, T. Miller, and T.-C. Chiang, Appl. Phys. Lett. **85**, 1235 (2004).
[47] P. Czoschke, H. Hong, L. Basile, and T.-C. Chiang (2005), (in press).
[48] I. K. Robinson and D. J. Tweet, Rep. Prog. Phys. **55**, 599 (1992).
[49] R. Feidenhans'l, Surf. Sci. Rep. **10**, 105 (1989).
[50] I. K. Robinson and E. Vlieg, Surf. Sci. **261**, 123 (1992).
[51] J. Als-Nielsen and D. McMorrow, *Elements of Modern X-Ray Physics* (John Wiley & Sons, Chichester, 2001).
[52] E. D. Specht and F. J. Walker, J. Appl. Cryst. **26**, 166 (1993).
[53] P. Marchand and L. Marmet, Rev. Sci. Instrum. **54**, 1034 (1983).
[54] D. A. Ricci, T. Miller, and T.-C. Chiang, Phys. Rev. Lett. **93**, 136801 (2004).